

# Asymmetrical Chirality in 3D Bended Metasurface

Ruhao Pan, Zhe Liu, Wei Zhu, Shuo Du, Changzhi Gu,\* and Junjie Li\*

Chiral metasurfaces offer crucial opportunities to expand the application potential for chiral photonics, but its desired freely structural control and giant circular dichroism (CD) allow for more and greater challenges. Here, different from previous metasurfaces with single structural regulation, a kind of bifunctional chiral metasurface based on 3D bended asymmetric construction is proposed, which shows giant CD combined with asymmetric chirality at 5.2  $\mu\text{m}$ . The bended metasurface with abundant spatial freedom, consisting of an array of asymmetric bended split ring resonators (SRRs), can be built up from the tensile stress induced by focused ion beam (FIB)–matter interaction. The results show that the CD increases with the bending angle of the metasurface and reaches a maximum at a bending angle of 60°. Particularly, it is found that the CD is 0.71/0.85 (experiment/simulation) for the backward incidence but  $-0.29/-0.29$  for the forward incidence, indicating that the giant CD and asymmetric chirality properties are realized simultaneously in the same metasurface. The calculated results of near-field distribution and the electric/magnetic dipoles show that the giant CD and the asymmetric chirality come from  $\vec{p} \cdot \vec{m} \neq 0$  and  $|\vec{p} \times \vec{m}| \neq 0$ , respectively. The findings inspire a high efficiency approach to design multifunctional chiral optical devices.

## 1. Introduction

Chiral materials, which refer to those for which one enantiomer cannot superimpose with its mirror enantiomer, are widespread in nature, such as kinds of amino acids and proteins.<sup>[1]</sup> More importantly, chiral materials present ways to modulate spin states of light due to the interactions between chiral matters and light with left-handed circular polarization (LCP) or its right-handed counterpart (RCP), such as circular dichroism (CD), or optical activities.<sup>[2]</sup> Among the chiroptical properties, CD is the differential transmission of LCP and RCP, which

comes from the different chiral responses. However, limited by the weak light-matter interaction, the chiroptical properties of natural materials are usually too weak for practical applications.<sup>[3]</sup> Fortunately, the optical metasurfaces, composed of artificial sub-wavelength structures, possess exotic properties in regulating the amplitude and phase of the electromagnetic wave, providing an efficient way to modulate the chiral light based on flexible pattern design.<sup>[4]</sup>


Recently, a series of chiral metasurfaces have been proposed to manipulate the spin states of the electromagnetic waves<sup>[5]</sup> and broadly applied as optical devices including circular polarizers, biosensors, and chiral light imaging.<sup>[6]</sup> Furthermore, chiral metasurface is expected to have more functions and applications including all-optical devices, optical information storage, and communication, and even quantum calculating devices,<sup>[7]</sup> but a multifunctional chiral metasurface is rarely reported so far due to the limitation of design and micro/nanofabrication.<sup>[8]</sup>

Previous reports have found the asymmetric transmission properties of chiral metasurfaces worked in various operating frequencies,<sup>[9,10]</sup> but their absolute values of CD are equivalent for the forward and backward incidence. Here, asymmetric transmission refers to the transmission difference of opposite incident directions for the light with certain polarizations.<sup>[11,12]</sup> If the absolute values of CD for the forward and backward incidence are different, it will result in an asymmetric chirality effect in chiral metasurfaces that is helpful to realize multifunctional chiral metasurface, but there have been no related reports so far. Combined asymmetric chirality with giant CD of metasurface will endow more abilities in realizing the control of optical logic devices, asymmetric circular polarizers, one-side chiral sensing, and spin-dependent light emission.<sup>[11,13]</sup>

The high performances of the chiral metasurfaces put forward higher request to the fabrication with abundant spatial controllability. The 2D chiral metasurfaces usually show small CDs limited to the lack of controllable degrees along z-axis,<sup>[9,14]</sup> while 3D configurations offer more opportunities to make up this shortfall, also showing higher CD, more functionalities, and stronger non-reciprocal behaviors.<sup>[15]</sup> However, these 3D metasurfaces are difficult to be achieved in mid-infrared band for the limitations in fabrication. Thus, to realize a perfect design of 3D chiral metasurface rely on powerful micro/nanofabrication. Traditionally, the 3D structures can be typically built up by 3D print or multilayer stack, however, these methods faces with problems in large feature sizes, long processing time and

Dr. R. Pan, W. Zhu, S. Du, Prof. C. Gu, Prof. J. Li  
Beijing National Laboratory for Condensed Matter Physics  
Institute of Physics  
Chinese Academy of Sciences  
Beijing 100190, China  
E-mail: czgu@iphy.ac.cn; jjli@iphy.ac.cn

Dr. Z. Liu  
Niels Bohr Institute  
University of Copenhagen  
Blegdamsvej 17, Copenhagen DK-2100, Denmark  
Prof. J. Li  
Songshan Lake Materials Laboratory  
Dongguan  
Guangdong 523808, China

 The ORCID identification number(s) for the author(s) of this article can be found under <https://doi.org/10.1002/adfm.202100689>.

DOI: 10.1002/adfm.202100689

complex processes.<sup>[16]</sup> Recently, some origami methods based on the folding and bending of the 2D films have been reported, such as Miura origami, compression buckling, residual stress induced bending, or even capillary force bending,<sup>[17]</sup> which demonstrates a flexible approach in 3D fabrication. Among the origami arts, focused ion beam (FIB)-defined origami shows strong fabrication capability and can be used to fabricate nanoscale structures with abundant degrees of spatial freedom and various materials,<sup>[18,19]</sup> and further origami-based 3D metasurface with Fano resonance, toroidal moment, and circular dichroism, have been designed and investigated.<sup>[20]</sup> Thus, the FIB defined origami meets more higher requirements of 3D metasurface structures, such as more degrees of freedom, smaller feature sizes, more compact configurations, and more complex functionalities, especially for the applications in the multifunctional and multiplexed photonic devices.<sup>[21]</sup>

In this work, based on the FIB defined origami fabrication, we propose one new 3D bended metasurface and demonstrate experimentally its giant asymmetric chirality in the mid-infrared range. Electron beam lithography (EBL) and electron beam deposition (EBD) are used to prepare the asymmetric split ring resonators (SRRs). Then, the global irradiation of FIB is applied to the planar patterns; a tensile stress in the surface layer of the cantilevers can be obtained due to the grain coalescence and the vacancy defects introduced by FIB-matter interaction; bended

metasurfaces are fabricated, where the bending angle can be flexibly tuned by the ion dose. Because of the asymmetric configuration, the near field electric field and surface current of the metasurface for the incident light with different spin states and incident directions display totally different distributions, which leads to an asymmetric chirality of the metasurface. The asymmetry can be tuned by bending angle, where the CD reaches a maximum of 0.71/0.85 (experimental/simulated) for the resonators with 60° bending angle and backward incidence, while for the forward incidence, the CD is −0.30/−0.29 (experimental/simulated). The results indicate that the CD is asymmetric for the forward and backward incidence, and a giant CD of 0.71 can be observed experimentally. Moreover, two configurations mirroring each other have been designed, in which complementary chiroptical response has been observed. Our work not only provides an approach to the simultaneous realization of giant CD and asymmetric chirality in the same metasurface, but also to enable 3D metasurfaces to have more potentials toward multifunctional chiral optical devices.

## 2. Results and Discussion

The schematic of 3D bended metasurface is illustrated in Figure 1a, composing asymmetric bended SRRs and a  $\text{SiN}_x$

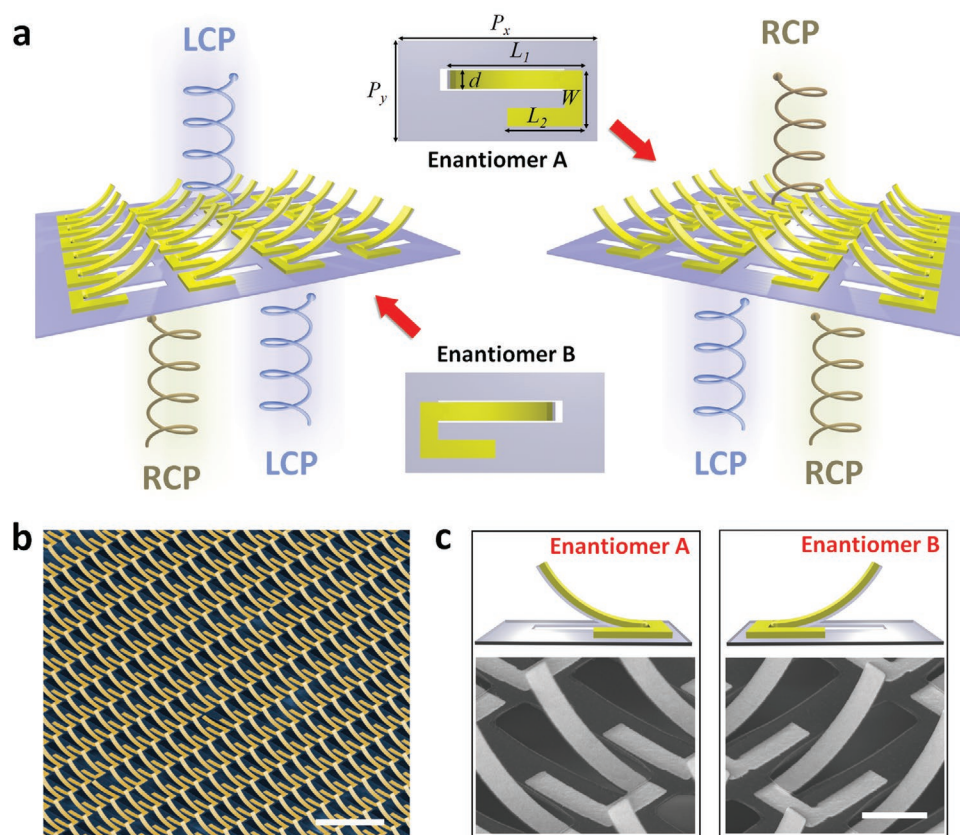


**Figure 1.** The schematic and fabrication of the 3D bended metasurface. a) Schematic of the bended metasurface. The critical sizes of asymmetric SRR, where the periods are  $P_x = 2 \mu\text{m}$  and  $P_y = 4 \mu\text{m}$ , and  $d$ ,  $w$ ,  $L_1$ , and  $L_2$  are 0.5, 1.5, 3.2, and 1.6  $\mu\text{m}$ , respectively. The structures are made of Au/SiN<sub>x</sub> film with a thickness of 80 nm/20 nm; b) Scanning electron microscope (SEM) image of a large array of bended metasurface; c) The schematic and SEM image of two types of the chiral enantiomers labeled as A and B. Scale bars: b) 10  $\mu\text{m}$  and c) 1  $\mu\text{m}$ .

frame. This asymmetric metasurface can show a spin selective transmission effect at the mid-infrared range, and the spin-selective property is inversed by the mirrored structure units of the metasurface. The key feature sizes are marked in Figure 1a, where the period of the metasurface is  $P_x = 2 \mu\text{m}$  and  $P_y = 4 \mu\text{m}$ . The SRR shows an asymmetric configuration, where  $w$ ,  $L_1$ , and  $L_2$  are  $1.5 \mu\text{m}$ ,  $3.2 \mu\text{m}$ , and  $1.6 \mu\text{m}$ , respectively, and the linewidth of the SRR is  $d = 0.5 \mu\text{m}$ . The planar asymmetric SRRs can be fabricated by the electron beam lithography (EBL) and metal thin film deposition. Then EBL is applied again to expose the margin pattern around the longer edge of the SRRs on  $\text{SiN}_x$  film, which is removed by subsequent reaction ion etching (RIE) to obtain suspended cantilevers. Significantly, mask lithography methods can be used to write the planar patterns for FIB irradiation, only if it can meet the requirement of the smallest line-width of the patterns. The 3D metasurface can be finally built up from the planar SRRs due to the tensile stress introduced by FIB global irradiation. When the cantilevers are globally irradiated by FIB, there are many phenomena that happen to the bilayer film including surfacing sputtering, ion-implantation, local disordering, grain coalescence, and vacancy defect. In the surface layer, a large tensile stress can be obtained because of the massive vacancy defects and grain coalescence,<sup>[21,22]</sup> which would bend the 2D films to 3D structures and hence the 3D metasurfaces are fabricated.<sup>[19]</sup> Figure 1b shows an array morphology of large area bended metasurface, where a uniform matrix of meta-atoms can be seen. The 3D structures can be bent into 2 types of chiral enantiomers by simply exchanging the position of the longer and shorter edges, and the two enantiomers are labeled as enantiomer A and enantiomer B, as shown in Figure 1c.

Due to the complementary properties of enantiomer A and enantiomer B, we will focus on enantiomer A in the following discussion, but it should be pointed out that the discussion can be applied to enantiomer B with exchanged spin state incidence. The bending angle ( $\theta$ ) is defined by  $\theta = 180 \times L_1/r$ , where  $L_1$  and  $r$  are the length and the curvature radius of the bended cantilever (Figure 2a), respectively, where  $\theta$  can be tuned by the curvature of the cantilever. Experimentally, the degree of symmetry breaking, which is dependent on the bending angle, can be continuously tuned by the ion dose of FIB irradiation. In order to fully investigate the performance of the bended metasurface with chiral configuration, the transmitted spectra for metasurfaces with different bending angles have been simulated by the finite elements method (FEM), and the results are shown in Figure 2. The total transmission of the metasurface can be

described by a matrix:  $t = \begin{pmatrix} t_{RR} & t_{RL} \\ t_{LR} & t_{LL} \end{pmatrix}$ , where  $t_{RR}/t_{LR}$  is the co-

polarized/cross-polarized transmission coefficient for RCP incidence, and  $t_{LL}/t_{RL}$  is the co-polarized/cross-polarized transmission coefficient for LCP incidence, respectively.<sup>[23]</sup> The intensity transmission of the RCP and LCP incidence are expressed by  $T_R = |t_{RR}|^2 + |t_{LR}|^2$  and  $T_L = |t_{RL}|^2 + |t_{LL}|^2$ . Figure 2a–c shows the schematic image, the LCP and the RCP transmission for forward incidence. Although the transmission spectra show little difference for LCP and RCP of the unbended metasurface, the bending of the metasurface breaks the mirror symmetry and leads to a chiral optical resonance, and provides transmittance

of one spin state while blocking the opposite one. For RCP incidence, a dip at  $\approx 5 \mu\text{m}$  can be observed and redshifted with the increase of the bending angle. However, for the LCP incidence, a broad peak appears at  $\approx 5 \mu\text{m}$ . The difference between  $T_R$  and  $T_L$  leads to a circular dichroism (CD), while the CD is relatively low compared to the reported works.<sup>[23,24]</sup> Fortunately, for the backward incidence, as shown in Figure 2d–f, the transmission for the LCP and RCP is greatly separated. This leads to the CD of backward incidence being much larger than the forward incident one. The differences in the transmission spectra and the CD indicate an asymmetric chirality property in this bended metasurface. Notably, the working wavelength of the bended metasurface is set to mid-infrared range that is the band of the characteristic peaks of many chiral macromolecules, certainly which can be also shortened by reducing the feature sizes of the metasurfaces.

In order to quantitatively analyze the chiroptical properties of the metasurface, the CD is defined by  $\text{CD} = T_R - T_L$ ,<sup>[25]</sup> as shown in Figure 2g. Both CDs for forward and backward incidence are calculated and shown in Figure 2h,i. For forward incidence, the CD is only 0.1 for the metasurface with 0 bending angle. However, with the angle increasing, the transmission difference between  $T_R$  and  $T_L$  increases. Due to the lack of symmetry breaking along  $z$ -axis, there is no asymmetric chirality for the metasurface with a bending angle of 0 (Figure S1, Supporting Information) for the forward and backward incidences. However, with the increase of the bending angle, the backward incidence generates a disparate transmission property compared to the forward incidence, namely the transmission of the RCP incidence is enhanced while that from LCP is weakened at  $\approx 5 \mu\text{m}$ . The CD increases fast with the bending angle, reaching a maximum of 0.85 when the bending angle is  $60^\circ$ . The asymmetric chirality results in an asymmetric CD, and the CD for forward incidence is only  $-0.29$  for the metasurface with  $60^\circ$  bending angle. The asymmetric CD is 0.56 in simulation, which is good enough for the application for optical logic devices, one-side sensing and single direction bio-sensing.

According to the simulated results, the  $60^\circ$  bended metasurfaces with the maximum CD are fabricated by the FIB defined origami (Figure 1b). Then Fourier transform infra-red spectrometer (FTIR) is used to characterize the transmission properties in the mid-infrared region. Figure 3a depicts the simulated transmission spectra of enantiomer A for LCP and RCP incidence, respectively, from which it can be clearly seen that  $T_L$  (red curve) is markedly larger than  $T_R$  (gray curve) from  $4.5$  to  $6 \mu\text{m}$ , and the CD reaches  $-0.29$ . Most importantly, the spin state dependent transmission is largely enhanced for the backward incidence. Figure 3b shows the simulated transmission from LCP and RCP incidence. Compared to the forward incidence, the resonance at  $5.2 \mu\text{m}$  provides a high transmission (0.87) for RCP incidence and a near zero transmission (0.02) for LCP, indicating a giant CD of 0.85 by simulation. The experimental results in Figure 3c,d confirm the simulated ones, where the line shapes of the transmission spectra for both the LCP and RCP incidence have a good agreement with the simulations, and the CD for the forward and backward incidence are  $-0.29$  (Figure 3c) and  $0.71$  (Figure 3d), respectively. The transmission spectra of enantiomer B are the complements of enantiomer A, where  $T_R$  is larger than  $T_L$  for forward incidence, and



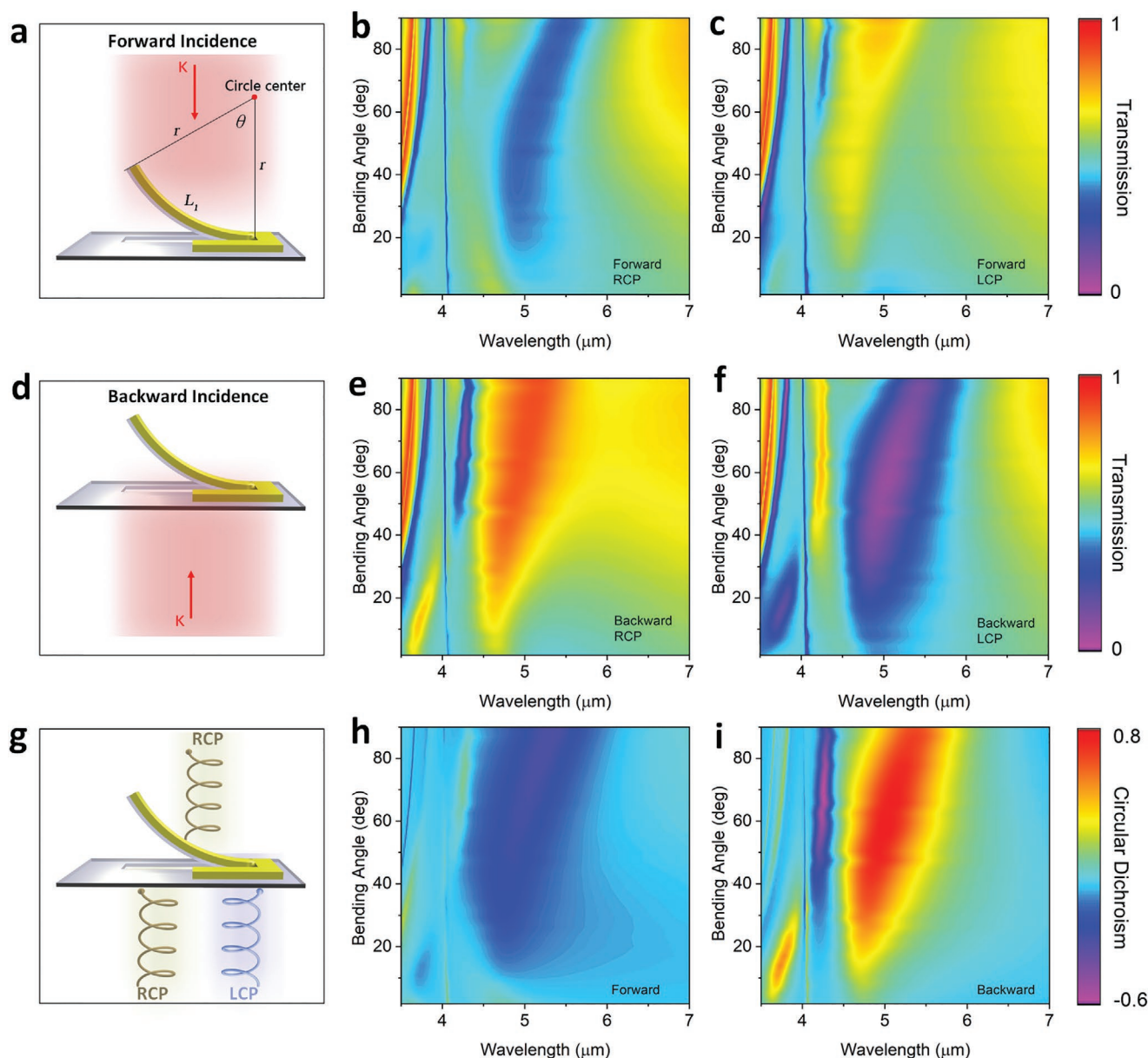


**Figure 2.** The chiroptical response of the 3D bended metasurface. a–c) The schematic and transmission of the metasurface with different bending angles for forward LCP and RCP incidence, respectively; d–f) The schematic and transmission of the metasurface with different bending angles for backward LCP and RCP incidence, respectively; g) Schematic of the spin state selected transmission of backward incidence, and the h,i) CD spectra of the RCP and LCP incidence.

$T_L$  is larger than  $T_R$  for backward incidence. Figure 3e,f depicts the experimental chiral transmission property of enantiomer B for the forward and backward incident, respectively, which shows similar line shapes with the spectra of enantiomer A after exchanging the polarizations of the incident light, and a giant CD of  $-0.67$  that is close to the simulation result can be obtained for the backward incidence.

The results mentioned above manifest that the 3D bended metasurface possesses giant CD and asymmetric chirality. However, the planar asymmetric SRR only shows a weak chiral resonance (Figure S1, Supporting Information) with symmetric transmission, which indicates that the large chiral modulation

ability and asymmetric chirality of the 3D bended metasurface rely on the mirror symmetry breaking of the bending configuration. The investigation of the underlined physics behind the chiroptical response helps the better understanding and applications of the chiral metasurface. The distribution of surface current and the near-field electric field of enantiomer A under the forward and backward incidences are extracted by FEM. Figure 4a shows the local current of the metasurface that was illuminated by the forward RCP, forward LCP, backward RCP, and backward LCP at  $5.2 \mu\text{m}$ , respectively, while their corresponding near field electric field distributions are shown in Figure 4b. It is easy to find that the direction and intensity of

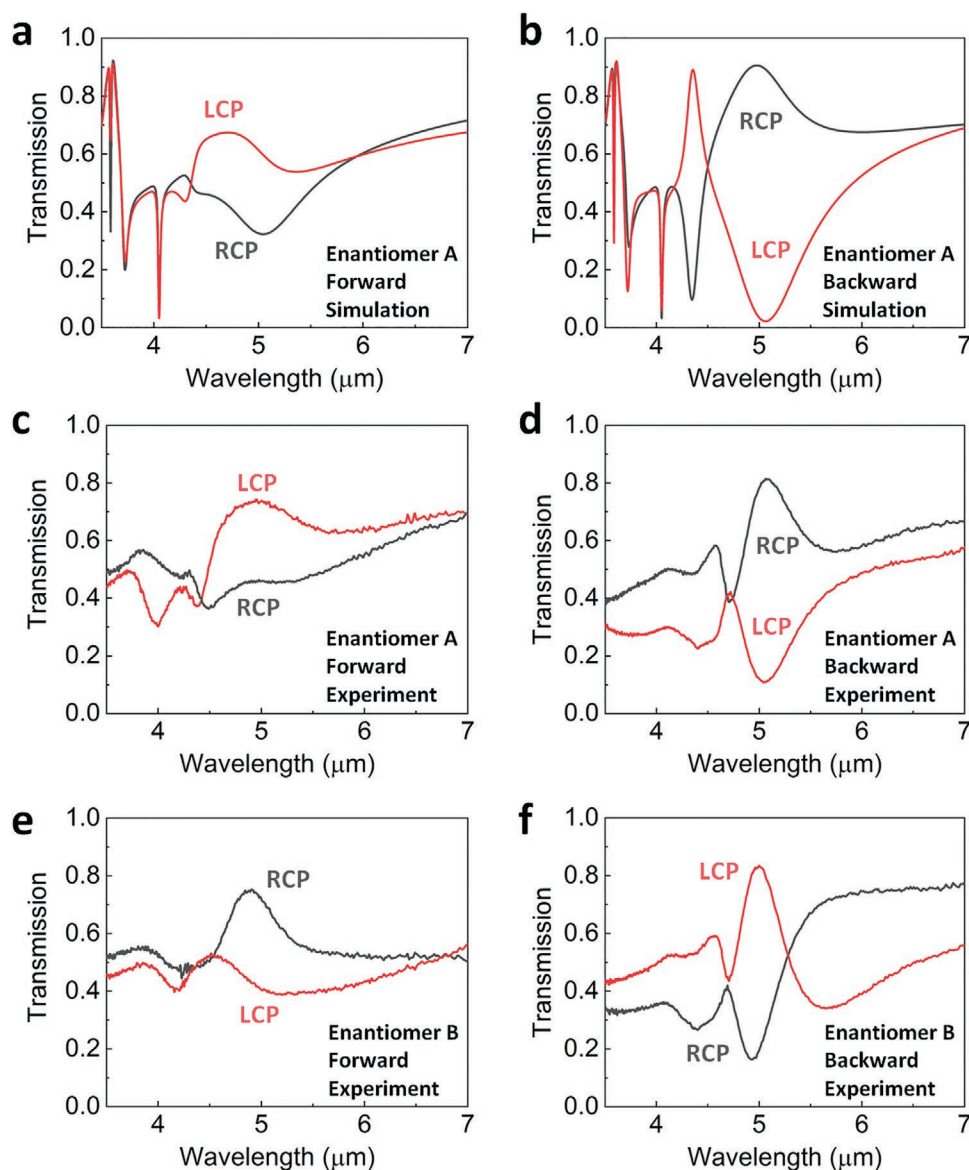


**Figure 3.** The transmission property of the metasurface with 60° bending angle. a) Simulated transmission spectra of enantiomer A for the forward incidence; the red and the gray curves indicate the RCP and LCP incidence, respectively. b) Simulated transmission spectra of enantiomer A for the backward incidence. c,d) The experimental transmission spectra of enantiomer A for the forward and backward incidence. e,f) The experimental transmission spectra of enantiomer B for the forward and backward incidence.

the surface currents bring out obvious distinctions for different incidences. According to Figure 4a, when the surface currents are excited by forward illumination, although the current directions are the same for both LCP and RCP incidence, the current density of the RCP incidence is much larger than that of LCP incidence, which leads to a weak transmission of RCP at 5  $\mu\text{m}$ , as shown in Figure 3c. As for the backward incidence, the current directions on the arms are distinctly different from the current that is excited by the forward incident light. It is worth noting that although the current directions of the backward LCP and RCP incidence are the same, the current density of RCP is too weak to influence the transmission. The local electric field, which is determined by the surface current, can directly reflect the resonance in the metasurface.<sup>[26]</sup> As

shown in Figure 4b, we can see the electric field of the backward LCP incidence is much stronger than the others, which results in the low transmission of the backward incident LCP, as shown in Figure 3d. The electric field of the forward RCP incidence is also stronger than the forward LCP incidence, which leads to the low transmission of the RCP incidence. The high absorption of the backward-incident LCP also results in a weak transmission of the electromagnetic wave, as shown in Figure S2, Supporting Information; the absorption of the backward incident LCP is higher than that obtained from the other incidences.

The chiral response comes from the interaction between the electric and the magnetic dipoles, the electric dipole ( $p$ ) and the magnetic dipole ( $m$ ) can be expressed by:

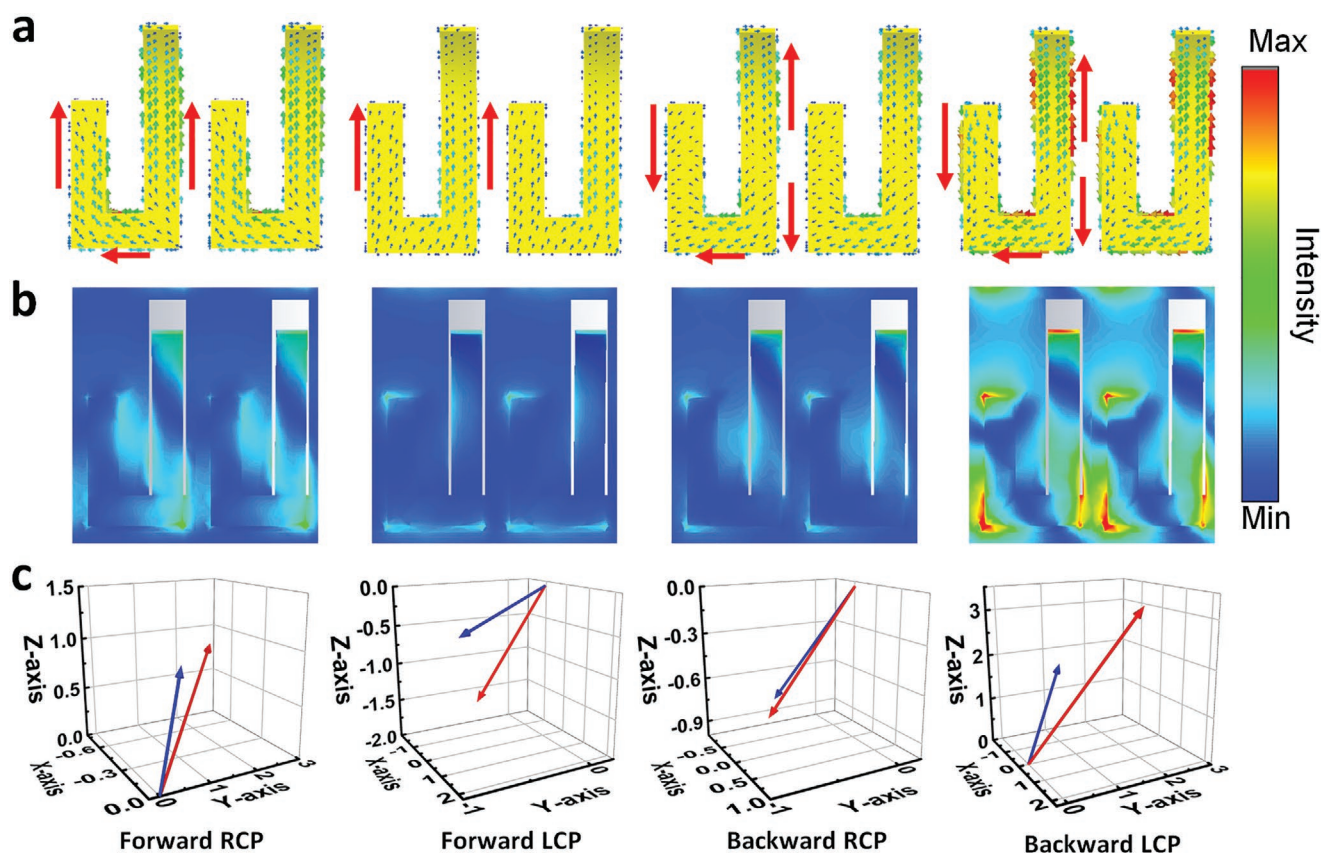


**Figure 4.** The near field distribution and direction of the electric/magnetic dipoles of the metasurface with 60° bending angle. a) The surface current, b) local electric field distribution, and c) dipole directions of enantiomer A for forward RCP, forward LCP, backward RCP, and backward LCP incidence, respectively.

$$\begin{cases} \vec{p} = p_{\text{eff},x} \cdot \hat{x} + p_{\text{eff},y} \cdot \hat{y} + p_{\text{eff},z} \cdot \hat{z} \\ \vec{m} = m_{\text{eff},x} \cdot \hat{x} + m_{\text{eff},y} \cdot \hat{y} + m_{\text{eff},z} \cdot \hat{z} \end{cases} \quad (1)$$

where  $p_{\text{eff},i}$  and  $\hat{i}$  are the effective electric field strength and unit vector along  $i(=x,y,z)$  direction, while  $m_{\text{eff},i}$  is the effective magnetic field strength. Only if  $\vec{p} \cdot \vec{m} \neq 0$ , the structure can show chiroptical response, while the asymmetric transmission can be observed for  $|\vec{p} \times \vec{m}| \neq 0$ .<sup>[23]</sup> The dipoles are calculated by the surface current, and Figure 4c depicts the directions of  $\vec{p}$  and  $\vec{m}$ , where we can see the electric and magnetic dipoles are pointed to different directions for different incidences due to the spatial configuration, and it is apparent that  $\vec{p} \cdot \vec{m} \neq 0$  and  $|\vec{p} \times \vec{m}| \neq 0$ , the circular dichroism and asymmetric transmission can be observed in the asymmetric resonators.<sup>[14]</sup>

Most importantly, the circular dichroism and asymmetric transmission of the metasurface also result in an asymmetric chirality. Here, the transmission matrix can be written as:

$$\mathbf{t}^+ = \begin{pmatrix} t_{RR}^+ & t_{RL}^+ \\ t_{LR}^+ & t_{LL}^+ \end{pmatrix} \text{ and } \mathbf{t}^- = \begin{pmatrix} t_{RR}^- & t_{RL}^- \\ t_{LR}^- & t_{LL}^- \end{pmatrix} \quad (2)$$

where “+” and “−” indicate the forward and backward incidence. The transmission coefficients are calculated and shown in Figure S3, Supporting Information. According to the Lorentz

reciprocity, the transmission coefficients satisfy the following relations:<sup>[8]</sup>

$$\begin{cases} t_{RR}^+ = t_{LL}^- \\ t_{LL}^+ = t_{RR}^- \\ t_{LR}^+ = t_{LR}^- \\ t_{RL}^+ = t_{RL}^- \end{cases} \quad (3)$$

Then,  $\mathbf{t}^-$  matrix can be written as  $\mathbf{t}^- = \begin{pmatrix} t_{LL}^+ & t_{RL}^+ \\ t_{LR}^+ & t_{RR}^+ \end{pmatrix}$ , and the

CD for the forward and backward incidence can be expressed by:

$$\text{CD} = \begin{cases} (|t_{RR}^+|^2 + |t_{LR}^+|^2) - (|t_{RL}^+|^2 + |t_{LL}^+|^2) & \text{(Forward)} \\ (|t_{LL}^+|^2 + |t_{LR}^+|^2) - (|t_{RL}^+|^2 + |t_{RR}^+|^2) & \text{(Backward)} \end{cases} \quad (4)$$

It is not difficult to find that the chirality of the bended metasurface is asymmetrical at different incident directions.

In order to intuitively observe the asymmetric CD, the CD spectra of the metasurface is calculated and experimentally characterized. Figure 5a shows the CD spectrum of the forward incidence, where the red and gray curves indicate the experiment and simulation. Both curves show the same line shape, and the CD at 5  $\mu\text{m}$  reaches  $-0.29/-0.29$  by simulation/experiment. Meanwhile, the CD for backward incidence is largely



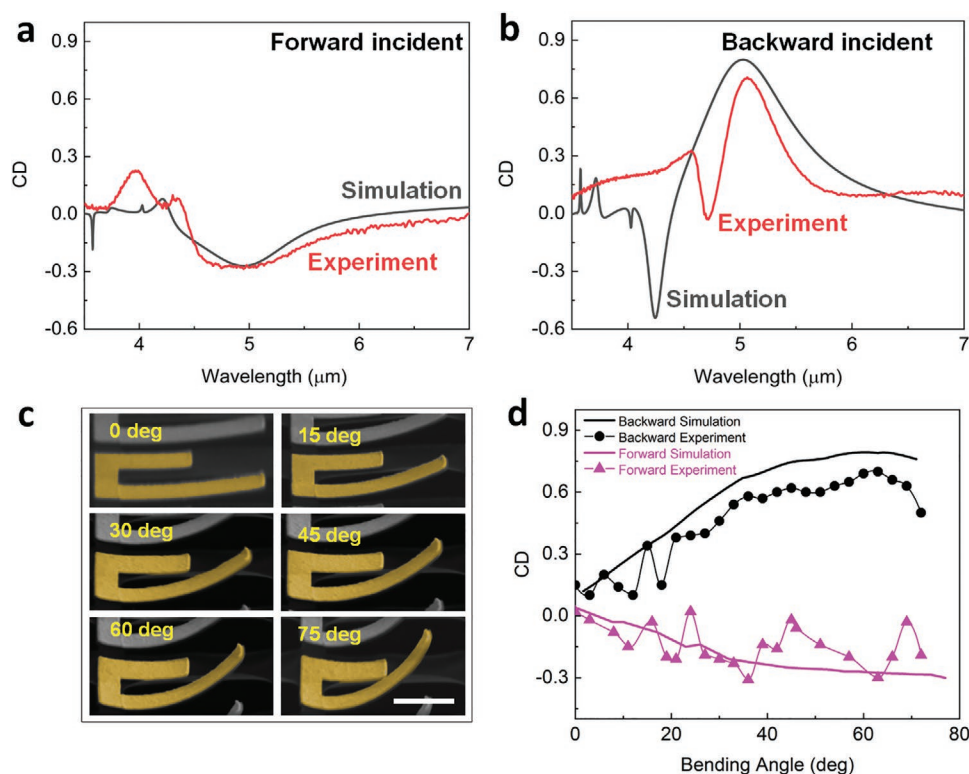


**Figure 5.** The asymmetric CD of the bended metasurface. a,b) The simulated (gray curve) and the experimental (red curve) of enantiomer B for forward and backward incidence, respectively; c) Metasurfaces with 0°, 15°, 30°, 45°, 60°, and 75° bending angles, which can be fabricated by different ion dose of FIB irradiation; d) The experimental and simulated CD at the resonance position as functions of bending angle for both forward and backward incidence. Scale Bar: 1 μm.

enhanced compared to the forward incidence, which originates from the disparate surface current and electric field distribution brought by the asymmetric configurations. As Figure 5b shows, the CD maximum appears at 5.1 μm, with a simulated and measured value of 0.85 and 0.71, respectively. The asymmetric CD reaches 0.41 by experiment. More importantly, the bending angle of the cantilever is the key parameter of the chiroptical response, and the CD for the metasurfaces with different bending angles are further investigated. The metasurfaces with different bending angles can be fabricated by tuning the ion dose of the FIB global irradiation, and the metasurfaces with 0, 15°, 30°, 45°, 60°, and 75° bending angles are displayed in Figure 5c. Figure 5d shows the CD at the resonance position as a function of the bending angle, where the simulated and experimental CDs yield to the same tendency. For forward incidence, as the pink curve shows, the absolute value of CD increases with the bending angle all the way down, while for backward incidence, the CD increases until it reaches a maximum at 60°. Both the CD and the transmission can be tuned in this 3D metasurface, and the differences between the simulations and the experiments come from the imperfection in the fabrication and the deviation in the measurement.

Limited by the controllable spatial degrees, as-reported 2D chiral metasurfaces usually show the CD values of smaller than 0.5 due to the restricted electromagnetic modes.<sup>[27]</sup> Thus, 3D configurations have been used in chiral metasurfaces, such as multi-layer metasurfaces, helix metasurfaces, and origami

metasurfaces. Although the CDs with more than 0.5 have been achieved, the directions of  $\vec{p}$  and  $\vec{m}$  are parallel/antiparallel, indicating the absolute values of the CD for the forward and backward incidence are always the same.<sup>[24,28]</sup> In this work, we have proposed a new type of 3D metasurface with giant asymmetrical chirality. Thanks to such complex 3D configurations, their electric and magnetic dipoles satisfy  $\vec{p} \cdot \vec{m} \neq 0$  and  $|\vec{p} \times \vec{m}| \neq 0$ , which results in not only a giant CD of 0.71 but also huge difference in the absolute values of the CD for forward and backward incidence.

### 3. Conclusion

In conclusion, this work proposes a new type of 3D bended chiral metasurface with asymmetric chirality and giant CD properties, which can be simply fabricated by FIB-based origami with global irradiation process. The symmetric breaking along z-axis results in the chiroptical responses, and the near fields for the different incidences show distinguished properties, and thus the transmission of the LCP and RCP waves has totally different line-shapes. According to the Lorentz reciprocity, the transmission for the forward and the backward incidence show different properties, and the CD at the forward incidence only reaches −0.29/−0.29 by simulation/experiment for the metasurface with 60° bending angle. However, the CD at the backward incidence reaches 0.8/0.71 by simulation/experiment,

indicating a strong chiroptical response. The simultaneous realization of giant CD and huge asymmetric chirality in the same 3D bended metasurface gives a good demonstration for multifunctional integration in optical chiral metasurface and also opens up a new horizon for the design of optical devices with complex functions.

## 4. Experimental Section

**2D Pattern Preparation:** The SiN<sub>x</sub> windows with 20 nm film were purchased (Ilabilab Company), and the area of the windows chosen was 100×100 μm<sup>2</sup>. First, these windows were cleaned under an oxygen plasma atmosphere by RIE for 10 s, and the pressure was maintained at 100 mTorr with 100 sccm O<sub>2</sub> flow. Then, PMMA (495 A5) was spin-coated on the windows, and 200 nm thick PMMA film was obtained after 180 °C bake. The PMMA was patterned by electron beam lithography (EBL) and then Au with a thickness of 80 nm was deposited by electron beam deposition to obtain as-patterned metal/dielectric bilayer on the windows. The further alinement lithography and RIE process were used to make the longer cantilever suspend, in which the etching duration of RIE process was 2 min under the power of 200 W, and the processing chamber maintained a 55 mTorr pressure with the gas flow of 5 sccm O<sub>2</sub> and 50 sccm CHF<sub>3</sub>. The residual PMMA was then removed by RIE. Finally, the asymmetric SRRs with free-standing cantilevers were obtained.

**FIB-Defined Origami:** The patterned bilayer membrane was placed into the chamber of a FIB/SEM system (Helios 600, FEI) with Ga ion source. The 2D asymmetric SRRs could be bended to a 3D structure by the ion irradiation process with area-scanning mode. Ion energy/current of 30 KeV/0.23 nA was applied to build up 3D metasurfaces. The in situ SEM system of the FIB/SEM system could be used to characterize the morphology of the 3D structures during the irradiation procedure. The bending angle ranges from 0 to 90° of the metasurface was determined by the ion dose of the FIB irradiation.

**Simulation:** FEM was implemented to optimize the structural parameters and analyze the near field properties of the designed bended metasurfaces. In the simulation, the thicknesses of the SiN<sub>x</sub> and Au films were set to 20 and 80 nm, respectively. And the boundary conditions in x and y directions were periodic. The wavelength of the light was from 3 to 8 μm. All the feature sizes and bending angles of the metasurfaces had been optimized to ensure the CD and asymmetric chirality to achieve the maximum. The near field current and electric field of the metasurface with 60° bending angle had been extracted.

**Optical Setup:** A Fourier-transform infrared spectrum (FTIR) system (Bruke Vetex V80) was used to measure the transmission and reflectance spectra of the metamaterials. This instrument was equipped with an NIR optical source. A sample with 100 × 100 μm<sup>2</sup> area was displaced under the microscope (Bruker Hyperion) with 15× objective lens. The background signal was obtained in air for 128 times scanning, and then the transmission spectra of the bended metasurfaces were obtained after 128 times scanning.

## Supporting Information

Supporting Information is available from the Wiley Online Library or from the author.

## Acknowledgements

The authors acknowledge the financial support received from the National Key Research and Development Program of China (Grant No. 2016YFA0200800 and 2016YFA0200400), the National Natural Science Foundation of China (Grant No. 12074420, 11674387, 91323304, and 61905274), China Postdoctoral Science Foundation (Grant No.

2020M670506), and the Key Research Program of Frontier Sciences of Chinese Academy of Sciences (Grant No. QYZDJ-SSW-SLH042). This work is also supported by the Synergic Extreme Condition User Facility.

## Conflict of Interest

The authors declare no conflict of interest.

## Data Availability Statement

Research data are not shared.

## Keywords

3D metasurfaces, asymmetric chirality, bended micro-configurations, electric resonance, magnetic resonance, giant circular dichroism

Received: January 21, 2021

Revised: April 6, 2021

Published online:

- [1] a) M. Khorasaninejad, W. T. Chen, A. Y. Zhu, J. Oh, R. C. Devlin, D. Rousso, F. Capasso, *Nano Lett.* **2016**, *16*, 4595; b) S. Garoff, R. B. Meyer, *Phys. Rev. Lett.* **1977**, *38*, 848; c) D. K. Kondepudi, G. W. Nelson, *Nature* **1985**, *314*, 438.
- [2] a) O. Derin, M. Karaaslan, E. Ünal, F. Karadağ, O. Altıntaş, O. Kögöl, *Bull. Mater. Sci.* **2019**, *42*, 191; b) C. Chen, L. Gao, W. Gao, C. Ge, X. Du, Z. Li, Y. Yang, G. Niu, J. Tang, *Nat. Commun.* **2019**, *10*, 1927.
- [3] H. Bui, S. A. Díaz, J. Fontana, M. Chiriboga, R. Veneziano, I. L. Medintz, *Adv. Opt. Mater.* **2019**, *7*, 1900562.
- [4] a) I. Fernandez-Corbaton, C. Rockstuhl, P. Ziemke, P. Gumbsch, A. Albiez, R. Schwaiger, T. Frenzel, M. Kadic, M. Wegener, *Adv. Mater.* **2019**, *31*, 1807742; b) V. K. Valev, J. J. Baumberg, C. Sibilia, T. Verbiest, *Adv. Mater.* **2013**, *25*, 2517; c) A. M. Shaltout, V. M. Shalae, M. L. Brongersma, *Science* **2019**, *366*, 364.
- [5] a) M. Esposito, V. Tasco, M. Cuscunà, F. Todisco, A. Benedetti, I. Tarantini, M. D. Giorgi, D. Sanvitto, A. Passaseo, *ACS Photonics* **2014**, *2*, 105; b) R. Verre, L. Shao, N. Odebo Lank, P. Karpinski, A. B. Yankovich, T. J. Antosiewicz, E. Olsson, M. Kall, *Adv. Mater.* **2017**, *29*, 1701352; c) L. Ouyang, W. Wang, D. Rosenmann, D. A. Czaplowski, J. Gao, X. Yang, *Opt. Express* **2018**, *26*, 31484.
- [6] a) N. A. Rubin, G. D'Aversa, P. Chevalier, Z. Shi, W. T. Chen, F. Capasso, *Science* **2019**, *365*, eaax1839; b) S. Jahani, Z. Jacob, *Nat. Nanotechnol.* **2016**, *11*, 23; c) Z. Liu, Z. Liu, J. Li, W. Li, J. Li, C. Gu, Z. Y. Li, *Sci. Rep.* **2016**, *6*, 27817.
- [7] W.-Z. Xu, Y.-T. Shi, J. Ye, F.-F. Ren, I. V. Shadrivov, H. Lu, L. Liang, X. Hu, B. Jin, R. Zhang, Y. Zheng, H. H. Tan, C. Jagadish, *Adv. Opt. Mater.* **2017**, *5*, 1600548.
- [8] Y. Chen, X. Yang, J. Gao, *Light: Sci. Appl.* **2019**, *8*, 45.
- [9] A. S. Schwanecke, V. A. Fedotov, V. V. Khaidikov, S. L. Prosvirnin, Y. Chen, N. I. Zheludev, *Nano Lett.* **2008**, *8*, 2940.
- [10] a) R. Singh, E. Plum, C. Menzel, C. Rockstuhl, A. K. Azad, R. A. Cheville, F. Lederer, W. Zhang, N. I. Zheludev, *Phys. Rev. B* **2009**, *80*, 153104; b) S. Wu, S. Xu, T. L. Zinenko, V. V. Yachin, S. L. Prosvirnin, V. R. Tuz, *Opt. Lett.* **2019**, *44*, 1056.
- [11] a) N. Parappurath, F. Alpegiani, L. Kuipers, E. Verhagen, *ACS Photonics* **2017**, *4*, 884; b) Z. Li, M. Mutlu, E. Ozbay, *J. Optics* **2013**, *15*, 023001.



- [12] a) C. Menzel, C. Helgert, C. Rockstuhl, E. B. Kley, A. Tunnermann, T. Pertsch, F. Lederer, *Phys. Rev. Lett.* **2010**, *104*, 253902; b) J. Dong, M. Wang, Y. Zhou, C. Zhou, Q. Wang, *Angew. Chem., Int. Ed.* **2020**, *59*, 15038; c) J. Li, P. Yu, C. Tang, H. Cheng, J. Li, S. Chen, J. Tian, *Adv. Opt. Mater.* **2017**, *5*, 1700152.
- [13] a) F. Zhang, M. Pu, X. Li, P. Gao, X. Ma, J. Luo, H. Yu, X. Luo, *Adv. Funct. Mater.* **2017**, *27*, 1704295; b) W. Liu, W. Wu, L. Huang, Y. Ling, C. Ba, S. Li, Z. Chun, H. Li, *Opt. Express* **2019**, *27*, 33399.
- [14] C. Liu, Y. Huang, F. Hu, Y. E. X. Dong, Y. Yang, Y. Jin, X. Xu, *Ann. Phys.* **2020**, *532*, 1900398.
- [15] M. Kadic, G. W. Milton, M. van Hecke, M. Wegener, *Nat. Rev. Phys.* **2019**, *1*, 198.
- [16] B. W. An, K. Kim, H. Lee, S. Y. Kim, Y. Shim, D. Y. Lee, J. Y. Song, J. U. Park, *Adv. Mater.* **2015**, *27*, 4322.
- [17] a) J. L. Silverberg, A. A. Evans, L. McLeod, R. C. Hayward, T. Hull, C. D. Santangelo, I. Cohen, *Science* **2014**, *345*, 647; b) J. W. Zeang Zhao, Xiaoming Mu, Haosen Chen, H. Jerry Qi, D. Fang, *Sci. Adv.* **2017**, *3*, e1602326; c) H. Fu, K. Nan, W. Bai, W. Huang, K. Bai, L. Lu, C. Zhou, Y. Liu, F. Liu, J. Wang, M. Han, Z. Yan, H. Luan, Y. Zhang, Y. Zhang, J. Zhao, X. Cheng, M. Li, J. W. Lee, Y. Liu, D. Fang, X. Li, Y. Huang, Y. Zhang, J. A. Rogers, *Nat. Mater.* **2018**, *17*, 268.
- [18] a) C. L. Wu, F. C. Li, C. W. Pao, D. J. Srolovitz, *Nano Lett.* **2017**, *17*, 249; b) C. Dai, J. H. Cho, *Nano Lett.* **2016**, *16*, 3655; c) A. Cui, Z. Liu, J. Li, T. H. Shen, X. Xia, Z. Li, Z. Gong, H. Li, B. Wang, J. Li, H. Yang, W. Li, C. Gu, *Light: Sci. Appl.* **2015**, *4*, e308.
- [19] R. Pan, Z. Li, Z. Liu, W. Zhu, L. Zhu, Y. Li, S. Chen, C. Gu, J. Li, *Laser Photonics Rev.* **2019**, *14*, 1900179.
- [20] a) J. Li, Z. Liu, *Nanophotonics* **2018**, *7*, 1637; b) Z. Liu, S. Du, A. Cui, Z. Li, Y. Fan, S. Chen, W. Li, J. Li, C. Gu, *Adv. Mater.* **2017**, *29*, 1606298; c) R. Pan, S. Du, Z. Liu, W. Zhu, C. Li, C. Gu, J. Li, *J. Optics* **2020**, *22*, 106103.
- [21] Z. Liu, H. Du, J. Li, L. Lu, Z.-Y. Li, N. X. Fang, *Sci. Adv.* **2018**, *4*, eaat4436.
- [22] W. D. Nix, B. M. Clemens, *J. Mater. Res.* **1999**, *14*, 3467.
- [23] Z. Wang, L. Jing, K. Yao, Y. Yang, B. Zheng, C. M. Soukoulis, H. Chen, Y. Liu, *Adv. Mater.* **2017**, *29*, 1700412.
- [24] A. Basiri, X. Chen, J. Bai, P. Amrollahi, J. Carpenter, Z. Holman, C. Wang, Y. Yao, *Light: Sci. Appl.* **2019**, *8*, 78.
- [25] S. Yang, Z. Liu, S. Hu, A. Z. Jin, H. Yang, S. Zhang, J. Li, C. Gu, *Nano Lett.* **2019**, *19*, 3432.
- [26] J. Cui, X. Ma, M. Pu, Y. Guo, X. Luo, *J. Optoelectron. Eng.* **2020**, *47*, 190052.
- [27] a) A. B. Khanikaev, N. Arju, Z. Fan, D. Purtseladze, F. Lu, J. Lee, P. Sarriugarte, M. Schnell, R. Hillenbrand, M. A. Belkin, G. Shvets, *Nat. Commun.* **2016**, *7*, 12045; b) S. Asgari, M. Rahmanzadeh, *Opt. Commun.* **2020**, *456*, 124623.
- [28] W. Ma, F. Cheng, Y. Liu, *ACS Nano* **2018**, *12*, 6326.